ADVANCED MATERIALS TECHNOLOGIES
www.advmattechnol.de

# Lithium All-Solid-State Batteries Fabricated at Room Temperature by the Powder Aerosol Deposition Method with Garnet-Type Electrolyte and Graded Composite Cathode

*Lukas Hennerici,* Paula Ficht, Maximilian Schamel, Ulrich Mansfeld, Mario Linz, Daniel Paulus, Jaroslaw Kita, Michael A. Danzer, and Ralf Moos**

**Lithium-based all-solid-state batteries (ASSBs) are attracting worldwide attention as the next step in the evolution of Li-ion batteries (LIBs). They have the potential to address safety concerns and limited energy densities, which are key challenges for LIBs. The current focus is on enhancing the electrochemical properties of ASSBs. However, a suitable economic method for fabricating them remains to be established, especially when ceramic materials are used as solid electrolytes. The powder aerosol deposition method (PAD or ADM) is a ceramic processing method that uses raw ceramic powders to fabricate dense, several micrometer thick ceramic films. The entire process takes place at room temperature and in the absence of additional binders. Therefore, PAD is used in this study to fabricate ASSBs with $LiNi_{0.83}Mn_{0.11}Co_{0.06}O_2$ (NMC) as the cathode active material and $Al_{0.2}Li_{6.025}La_3Zr_{1.625}Ta_{0.375}O_{12}$ (LLZO) as the solid electrolyte. The cathode is fabricated as a composite with a gradient in the electrolyte concentration. The successful fabrication is confirmed through scanning electron microscopy and energy-dispersive X-ray spectroscopy analysis. Electrochemical characterization shows that a PAD-ASSB can be cycled. Furthermore, it can be shown that 145 µm thick NMC films can be fabricated by PAD. The electrochemical results are compared with the theoretical potential of PAD-ASSBs, and methods to further improve the achieved state are discussed.**

## 1. Introduction

In the context of climate change and the necessary transition from fossil fuels to electrical energy sources, all-solid-state batteries (ASSBs) based on the Li-ion technology are promising future electrical energy storage devices. Replacing the liquid electrolyte used in commercial Li-ion batteries (LIBs) by a solid electrolyte may allow for increased safety and improved performance in terms of energy density as well as charging time.[1–4] As a result, the interest in research and industry has increased over the past decade, leading to a variety of different innovative approaches to enable the fabrication of a commercially viable ASSBs.[5–7]

As one of the new approaches, the powder aerosol deposition method (PAD), in literature also known as aerosol deposition method (ADM), has emerged as a method for film fabrication from raw powders especially for ceramic-based ASSBs. The PAD enables the fabrication of dense ceramic films directly at room temperature based on the room temperature impact consolidation (RTIC) mechanism.[8,9] The thickness of PAD films can range from a few µm to ≈100–200 µm depending on the utilized powder.[10,11] The PAD process and films offer several benefits for fabricating batteries. Starting with the process temperature, the fabrication cost of batteries could be drastically reduced using PAD, since the entire process takes place at

---

L. Hennerici, P. Ficht, M. Linz, D. Paulus, J. Kita, R. Moos
Department of Functional Materials
University of Bayreuth
Universitätsstraße 30, 95447 Bayreuth, Germany
E-mail: functional.materials@uni-bayreuth.de

The ORCID identification number(s) for the author(s) of this article can be found under https://doi.org/10.1002/admt.202400745

[Correction added on August 29, 2024, after first online publication: Email ID has been changed for both the corresponding authors.]

**DOI: 10.1002/admt.202400745**

L. Hennerici, M. Schamel, M. Linz, M. A. Danzer, R. Moos
Bayerisches Zentrum für Batterietechnik
Weiherstraße 26, 95448 Bayreuth, Germany

M. Schamel, M. A. Danzer
Chair of Electrical Energy Systems
University of Bayreuth
Universitätsstraße 30, 95447 Bayreuth, Germany

U. Mansfeld
Bavarian Polymer Institute (BPI)
University of Bayreuth
Universitätsstraße 30, 95447 Bayreuth, Germany

room temperature. Other commonly used fabrication processes for ceramic-based ASSBs with, e.g., an oxide electrolyte, such as tape casting, require significantly higher temperatures during the fabrication process (>1000 °C).[7,12] In addition to that, no supplementary processing additives are required. This simplifies material preparation and reduces process costs.[11] In terms of electrochemical performance, the PAD-ASSBs electrodes would make the use of binders obsolete, as PAD films generally exhibit very high adhesion.[13] This would not only remove poorly conductive binder material but also would allow for higher energy densities. The high density of PAD films, typically >95% of the bulk density (with no open porosity), would enable higher energy densities while eliminating the need for a postprocess densification step.[8,14] Besides that, the high density of PAD films would lead to higher particle-to-particle contact compared to other fabrication processes, resulting in lower interfacial resistance and reduced tortuosity.

To date, a wide variety of different materials already have been deposited and characterized using the PAD process. For cathode active materials (CAMs), the commercially used layered oxides $LiNi_{1-x-y}Mn_xCo_yO_2$ (NMC),[15–18] $LiCoO_2$,[19–21] and $LiFePO_4$ (LFP)[22–25] are mainly investigated. In the field of solid electrolytes the garnet-like $Li_7La_3Zr_2O_{12}$ (LLZO) has received most attention,[12,25–30] while there are only few studies present for other solid electrolytes, namely, $Li_{1.3}Al_{0.3}Ti_{1.7}(PO_4)_3$ (LATP),[31] $Li_{1.5}Al_{0.5}Ge_{1.5}(PO_4)_3$,[32,33] and $Li_{0.35}La_{0.55}TiO_3$[34] Si is the most investigated anode active material[35–42] followed by $Sn_4P_3$[43,44] and $Mg_2Ge$[35,45,46] Li metal, considered the most promising anode active material, cannot be deposited successfully with PAD due to its softness, making it unable to get densified by the RTIC mechanism.

Despite the numerous studies, up to now, it has only been demonstrated once that a subsequent PAD deposition of electrode and electrolyte film on a current collector substrate can act as ASSBs. Ahn et al. deposited an LFP-PAD film ($d = 1$ µm) on a stainless-steel substrate covered with an LLZO-PAD film ($d = 20$ µm) and finally applied a Li-foil as anode. Using a C-rate of 0.3 C at 140 °C, a gravimetric capacity of 53 mAh $g^{-1}$ was obtained.[25] Based on this study, several challenges can be identified that need to be addressed before PAD-ASSBs can be considered suitable for commercial use. One of them is the further development of the cell architecture, especially the cathode layer design. To enable energy densities higher than 300 Wh $kg^{-1}$ and 1000 Wh $L^{-1}$, a significantly thicker cathode layer, more than 1 µm, would be required. Additionally, the application of a composite cathode layer in which conductive additives are introduced into the cathode in ASSBs, is inevitable.[47] Different studies show that the microstructure of the composition of the cathode layer plays a crucial role for optimizing the performance of ASSBs.[48–50] Building on that, virtual simulation studies indicate that, in theory, layered or graded electrodes with an increased electrolyte concentration toward the separator can significantly enhance the electrode performance due to improved ionic transport.[51–53] Three approaches were made to fabricate a composite cathode using LATP as solid electrolyte and NMC,[16] $LiNi_{0.5}Mn_{1.5}O_4$[54] or LCO[20] as CAM, showing that in principle the fabrication of PAD composite cathodes is possible. However, these studies solely utilized the PAD to fabricate the cathode layer. When an electrolyte layer was added, a different fabrication process was used.

In this work, we aimed to further improve the cathode layer design of PAD-ASSBs, while using PAD as processing method for both cathode and electrolyte layers. For this, we used Ni-rich NMC ($LiNi_{0.83}Mn_{0.11}Co_{0.06}O_2$) as already commercially proven CAM, along with Al- and Ta-doped LLZO ($Al_{0.2}Li_{6.025}La_3Zr_{1.625}Ta_{0.375}O_{12}$), as one of the most promising oxide solid electrolyte materials. The fabricated ASSBs contained a gradient cathode layer, achieved by stepwise increasing the solid electrolyte concentration toward the electrolyte layer. The materials were individually studied as single layer films before a multilayer film was fabricated and investigated. The film compositions were analyzed using scanning electron microscopy (SEM) and energy-dispersive X-ray spectroscopy (EDX). Within this work, we also showed that the fabricated PAD-ASSBs with a graded cathode can be cycled. Based on these results, we compared the performance of the current state-of-the-art PAD-ASSBs to its theoretical potential by simulating possible energy densities. Finally, different methods to improve the electrochemical performance of the current state-of-the-art PAD-ASSBs were discussed.

## 2. Experimental Section

The experimental approach of this study is illustrated in **Figure 1**. Initially, the raw powders NMC and LLZO were deposited, and the films were subsequently characterized (step 1, 1.I, 1.II). In the next step, the PAD films of the composite materials were analyzed. Three different compositions, namely, 75:25 wt% NMC:LLZO (Composite 1), 50:50 wt% NMC:LLZO (Composite 2), and 25:75 wt% NMC:LLZO (Composite 3) were investigated (step 2, 2.I–III). In the third step, two multilayer films were fabricated and characterized, containing a cathode setup with a gradient (step 3, 3.I, 3.II). The respective films were deposited on $Al_2O_3$ substrates to investigate them in SEM and EDX. Finally, a film setup according to 3.I in Figure 1 was fabricated and covered with a Li-foil as anode for electrochemical characterization. A Hastelloy substrate was used as the current collector on the cathode side for step 4.

### 2.1. Powder Synthesis

#### 2.1.1. Cathode Material

Ni-rich NMC CAM with a composition of $LiNi_{0.83}Mn_{0.11}Co_{0.06}O_2$ was received from MSE supplies LLC. The received powder was ball milled for 35 min in cyclohexane. The solvent was evaporated at room temperature after milling. The powder was subsequently sieved with a mesh size of 90 µm, dried at 120 °C in a furnace, and stored in dry argon until further use.

#### 2.1.2. Solid Electrolyte Material

Al- and Ta-doped LLZO with the composition $Al_{0.2}Li_{6.025}La_3Zr_{1.625}Ta_{0.375}O_{12}$ was synthesized using the mixed-oxide route reported by Nazarenus et al.[12] The powder was stored in dry argon until further use.

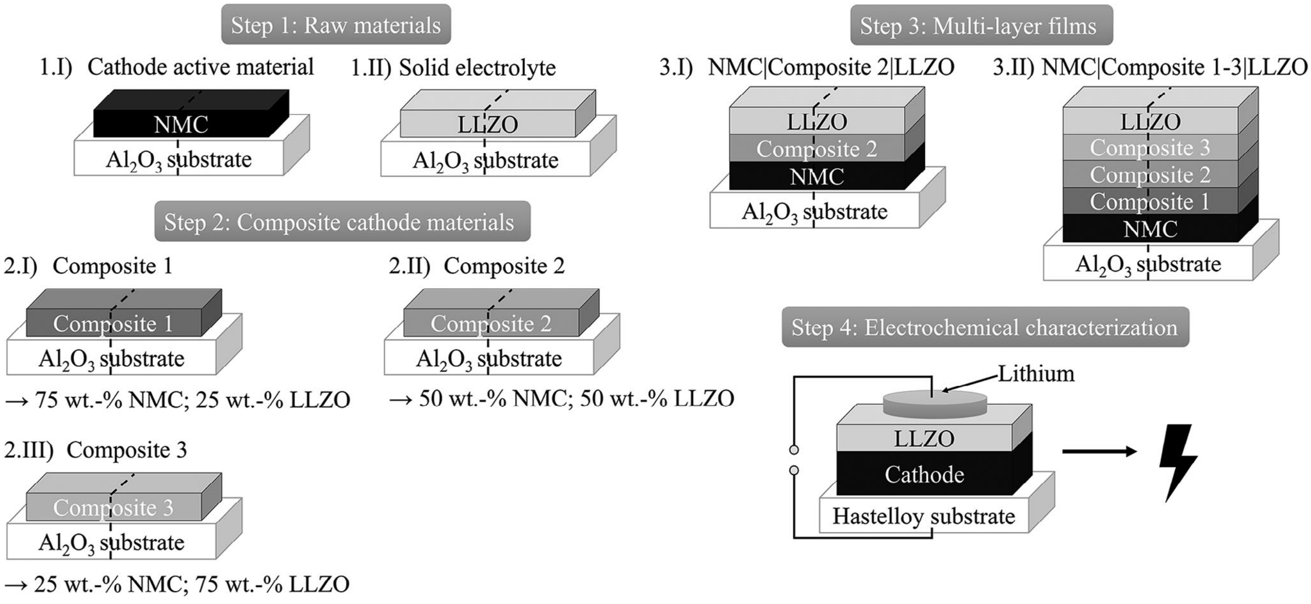

**Figure 1.** Experimental approach of this study: (step 1) analysis of the raw material PAD films: I) NMC (Cathode active material), II) LLZO (Solid electrolyte). (step 2) analysis and comparison of NMC/LLZO composite PAD films: I) 75:25 wt% NMC:LLZO (Composite 1), II) 50:50 wt% NMC:LLZO (Composite 2), III) 25:75 wt% NMC:LLZO (Composite 3). (step 3) fabrication and analysis of multilayer PAD films: I) NMC|Composite 2|LLZO, II) NMC|Composite 1|Composite 2|Composite 3|LLZO. (step 4) electrochemical characterization of a multilayer PAD-ASSB.

### *2.1.3. Cathode Composite Material*

To prepare Composite 1 (75:25 wt% NMC:LLZO), Composite 2 (50:50 wt% NMC:LLZO), and Composite 3 (25:75 wt% NMC:LLZO), the corresponding compositions were weighed, and the powders were ground in a mortar for homogenization. The prepared composites were stored in dry argon until further use.

## 2.2. Film Fabrication

The films were fabricated using a custom-made PAD apparatus, the working principle of which has been reported elsewhere.[11,12] Two types of aerosol generators were used (cf. **Figure 2**). To fabricate the cathode layer/film (NMC and composites), an aerosol chamber was placed on a vibrating table. An $O_2$ gas flow was used to generate the aerosol (Figure 2a). To fabricate the electrolyte layer/film, an aerosol generator was placed in a glovebox with inert $N_2$ atmosphere. A dispersing $O_2$ gas flow in the Venturi nozzle ensures that the ceramic particles are converted into a powder aerosol. Driven by the pressure gradient between glovebox and vacuum in the deposition chamber, the aerosol flows toward the nozzle and the particles are subsequently deposited on the substrate material (Figure 2b).

## 2.3. Sample Preparation

### *2.3.1. SEM and EDX*

For cross-sectional analysis, the deposited films on the $Al_2O_3$ substrate were bisected along a predefined breaking edge. The cross-section was dry polished with sandpaper without additive (1200 grit, SiC, 5 µm grain size) to obtain a plane surface with low roughness.

### *2.3.2. Electrochemical Characterization*

For electrochemical characterization, an NMC layer ($d \approx 15$ µm) and a Composite 2 layer ($d \approx 10$ µm) as cathode were consecutively deposited and covered with an LLZO layer ($d \approx 30$ µm) as electrolyte (cf. 3.I). The thickness of each individual layer was determined on an additional substrate. The additional substrates were coated in the same representative deposition step by extending the scanning distance to enable a representative measurement of coating thickness. The surface of the electrolyte was polished with sandpaper without additive (1200 grit, SiC, 5 µm grain size) to obtain a plane surface with low roughness and remove any impurities. Finally, a Li-metal anode (⌀3 mm, 0.75 mm thickness) was applied on top of the PAD film.

## 2.4. Characterization Methods

### *2.4.1. Scanning Electron Microscopy*

A Zeiss Leo Gemini 1530 (Carl Zeiss AG, Oberkochen, Germany) was used for SEM with SE and BSE imaging. An acceleration voltage of 3 keV for SE imaging and 10 keV for BSE imaging was applied. Additionally for the SEM–BSE imaging of the multilayer films 3.I and 3.II, an FEI Quanta FEG 250 (FEI Company, Hillsboro, OR, USA) with a concentric BSE detector was used (acceleration voltage 30 keV). All samples were coated with a conductive carbon layer that was ≈20 nm thick.

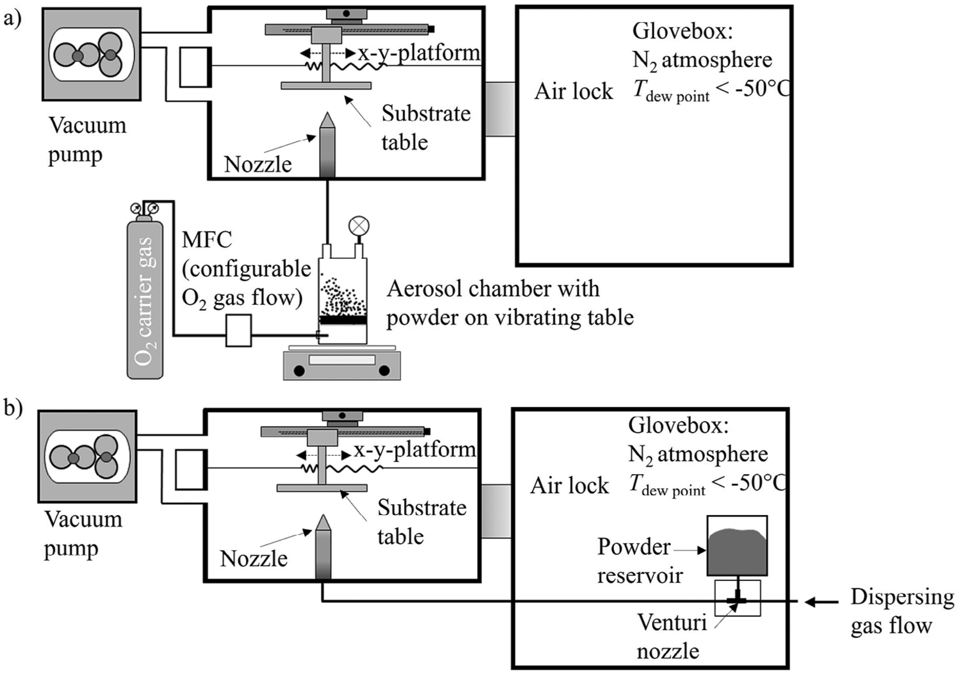

**Figure 2.** Schematic illustration of the PAD apparatuses used for film fabrication. a) PAD apparatus with aerosol chamber on a vibrating table as aerosol generating unit for cathode film fabrication. b) PAD apparatus with aerosol generator and venturi nozzle as aerosol generating unit for electrolyte film fabrication.[12] Reproduced under the terms of the CC-BY license.[12] Copyright 2021, Wiley-VCH.

#### *2.4.2. Energy-Dispersive X-Ray Spectroscopy*

EDX analysis was performed with a Thermo Fisher Scientific NS7 (Thermo Fisher Scientific Inc., Waltham, MA, USA; acceleration voltage 15 keV). The samples were coated with a conductive carbon layer that was ≈20 nm thick. Standardless EDX mapping and the quantitative analysis was performed with the Pathfinder version 2.8 (Thermo Fisher Scientific Inc., Waltham, MA, USA) software.

#### *2.4.3. Electrochemical Characterization*

The samples were electrochemically characterized in a CompreDrive system (rhd instruments, Darmstadt, Germany), allowing for active force and temperature control. The force was set to 0.03 kN throughout all experiments resulting in a pressure of ≈2.4 MPa. The electrochemical characterization was carried out at 70 °C. For galvanostatic cycling and electrochemical impedance spectroscopy (EIS), an Arbin LBTX20084 cell tester in combination with a Gamry Interface 1010E was used. EIS was conducted in galvanostatic mode with an amplitude of 1.5 µA within the frequency range of 10 kHz to 10 mHz with ten steps per decade.

#### *2.4.4. Surface Characterization*

To determine the thickness of the PAD films, a Mahr S2 Perthometer (Carl Mahr Holding GmbH, Göttingen, Germany) was utilized to obtain surface profiles.

## 3. Results and Discussion

### 3.1. Characterization of the PAD Films of the Raw Materials (Step 1)

The results of the SEM analysis in form of SE images as well as standardless EDX maps of the NMC- (1.I) and LLZO-PAD films (1.II) are shown in **Figure 3**. Standardless EDX was used to detect Ni (blue), Mn (cyan), and Co (orange) for NMC (Figure 3b) as well as Al (green), La (yellow), Zr (red), and Ta (violet) for LLZO (Figure 3d).

The SEM images show that dense films of several µm thickness could be deposited for both films. Yet, as a result of the polishing step before SEM analysis, the characteristic nanocrystalline morphology cannot be detected using SEM–SE imaging. The standardless EDX mapping for both films shows a homogenous distribution of almost all analyzed elements. Ta as part of LLZO could not be observed in the EDX mapping of the LLZO-PAD film (Figure 3b).

In order to determine the elemental composition of the PAD films, the molar fractions $\chi_i$ of the examined elements were calculated for both films using the standardless EDX data. The determined values for $\chi_i$ are shown in Tables S1 and S2 of the Supporting Information. Based on $\chi_i$, the elemental distributions of each material were estimated. For NMC, it was assumed that the sum of all $\chi_{\text{tot}}$ ($\chi_{\text{Ni}}$, $\chi_{\text{Mn}}$, $\chi_{\text{Co}}$) is 100 at% according to $\text{LiNi}_x\text{Mn}_y\text{Co}_z\text{O}_2$ ($x + y + z = 1$). By following this assumption, the amount of the respective element per formula $\dot{n}$ for the used NMC powder can be calculated using Equation (1)

$$\dot{n}\,(\text{Ni, Mn, Co}) = \frac{\chi_i}{\chi_{\text{tot}}} \tag{1}$$

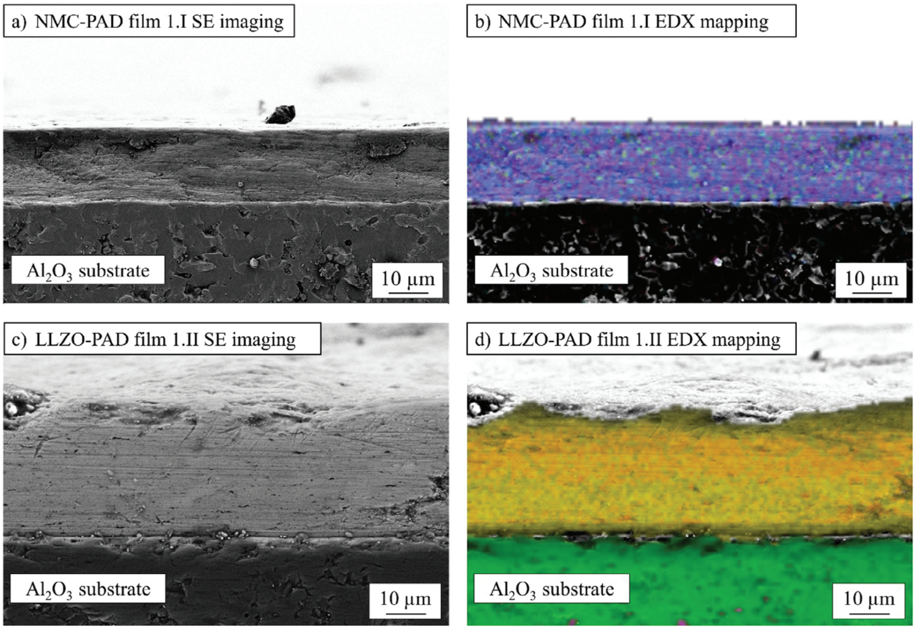

**Figure 3.** a) SE image of an NMC-PAD film (1.I) as cross-section. b) Standardless EDX mapping (Ni = blue, Mn = cyan, Co = orange) of an NMC-PAD film (1.I) as cross-section. c) SE image of an LLZO-PAD film (1.II) as cross-section. d) Standardless EDX mapping (Al = green, La = yellow, Zr = red, Ta = violet) of an LLZO-PAD film (1.II) as cross-section.

For LLZO, it was defined that the molar fraction of La equals 3 atoms per formula unit according to $Al_{0.2}Li_{6.025}La_3Zr_{1.625}Ta_{0.375}O_{12}$. From that, the amount of the respective element per formula unit $\dot{n}$ of the remaining elements can be calculated with Equation (2)

$$\dot{n}\,(\mathrm{Al},\ \mathrm{Ta},\ \mathrm{Zr}) = \frac{\chi_\mathrm{i}}{\chi_\mathrm{La}} \cdot 3 \tag{2}$$

The resulting film compositions are shown in **Table 1** for the NMC film and in **Table 2** for the LLZO film in contrast to the nominal compositions.

The composition of the NMC-PAD film is determined to be identical to the nominal composition of the raw material. For the LLZO-PAD film, the Al and Zr shares are in the range of the respective share in the nominal composition, while Ta could not be detected within the film. This result is consistent with the observation made for the mapping of the film in Figure 3d. One possible explanation for this observation is the inhomogeneous distribution of elements within the starting powder (Figure S1, Supporting Information), which shows that Ta is not uniformly distributed within the LLZO starting powder. Linz et al. have demonstrated that only a portion of the powder is deposited in the RTIC mechanism that occurs during the deposition process using PAD.[18] Consequently, it is plausible that only the Ta-poor phase within the powder is deposited during the film fabrication process. To substantiate this hypothesis, further investigation is necessary. However, this is beyond the scope of this study. Still, the SEM images and the standardless EDX data demonstrate the formation of dense and thick films of NMC and LLZO by PAD.

**Table 1.** Composition of NMC-PAD film 1.I calculated from standardless EDX analysis in contrast of the nominal one ($LiNi_{0.83}Mn_{0.11}Co_{0.06}O_2$).

| | $\dot{n}_\mathrm{Ni}$ [au] | $\dot{n}_\mathrm{Mn}$ [au] | $\dot{n}_\mathrm{Co}$ [au] |
|---|---|---|---|
| Nom. comp. | 0.83 | 0.06 | 0.11 |
| Film comp. | 0.83 | 0.06 | 0.11 |

### 3.2. Characterization of the PAD Films of the Composites (Step 2)

SEM–SE images and standardless EDX maps of the Composite 1 (2.I), Composite 2 (2.II), and Composite 3 (2.III) PAD films are shown in Figure S2a,c,e of the Supporting Information. Standardless EDX was used to detect only Ni and La to determine the proportion of NMC and LLZO in the films. The selection of Ni and La is because they have the largest mass fraction in the respective raw material. Equation (3) (for Composite 1 PAD film (2.I)) and Equation (4) (for Composite 2 (2.II) and 3 (2.III) PAD film) are used to determine the mass ratio of each material within the three composite PAD films

$$\frac{m_\mathrm{LLZO}}{m_\mathrm{NMC}} = \frac{\chi_\mathrm{La}}{\chi_\mathrm{Ni}} \cdot \frac{M_\mathrm{LLZO}}{M_\mathrm{NMC}} \cdot \frac{0.83}{3} \tag{3}$$

**Table 2.** Composition of LLZO-PAD film 1.II calculated from standardless EDX analysis in contrast of the nominal one ($Al_{0.2}Li_{6.025}La_3Zr_{1.625}Ta_{0.375}O_{12}$).

| | $\dot{n}_\mathrm{Al}$ [au] | $\dot{n}_\mathrm{La}$ [au] | $\dot{n}_\mathrm{Zr}$ [au] | $\dot{n}_\mathrm{Ta}$ [au] |
|---|---|---|---|---|
| Nom. comp. | 0.20 | 3.00 | 1.625 | 0.375 |
| Film comp. | 0.13 | 3.00 | 1.45 | – |

**Table 3.** Results of the standardless EDX analysis for the analysis of the Composite 1, Composite 2, and Composite 3 PAD film to determine the composition in respect to the proportion of LLZO and NMC within the film.

| Layer | $\chi_{\text{Ni K line}}$ [at%] | $\chi_{\text{La L line}}$ [at%] | Mass ratio (meas.) [au] | Mass ratio (nominal) [au] |
|---|---|---|---|---|
| Composite 1 | 76.50 | 23.50 | 1.3:1 | 3:1 |
| Composite 2 | 48.49 | 51.51 | 1:2.6 | 1:1 |
| Composite 3 | 24.23 | 75.77 | 1:7.7 | 1:3 |

$$\frac{m_{\text{NMC}}}{m_{\text{LLZO}}} = \frac{\chi_{\text{Ni}}}{\chi_{\text{La}}} \cdot \frac{M_{\text{NMC}}}{M_{\text{LLZO}}} \cdot \frac{3}{0.83} \tag{4}$$

The mass ratio determined for each PAD film is listed in **Table** 3, together with the desired mass ratio and the measured $\chi$ for Ni and La from the standardless EDX analysis.

The proportion of LLZO within the film appears to be higher than in the original composition of the starting powders. It may be assumed that the deposition of LLZO is favored using a composite powder consisting of NMC and LLZO. Here, either a higher deposition rate of LLZO or a higher powder discharge from the powder chamber may explain the higher LLZO proportion within the PAD films (cf. Figure 2a). Further analysis is required to determine the composition of PAD films more accurately in terms of NMC and LLZO concentration. Quantitative analytical methods such as inductively coupled plasma combined with optical emission spectroscopy, X-ray photoelectron spectroscopy or time-of-flight secondary ion mass spectrometry could be used.

However, the focus of this study is on a proof of concept for fabricating ASSBs with a graded cathode. Looking at the BSE images of the three composite films presented in Figure S2 b,d,f of the Supporting Information, it is evident that two different phases are present within the film. The BSE detector is sensitive to atomic mass. Therefore, the grayscale image displays LLZO as a brighter gray and NMC as a darker gray. Consequently, it is demonstrated that PAD is suitable to prepare films containing two phases using a composite powder of NMC and LLZO.

### 3.3. Characterization of the Multilayer PAD Films (Step 3)

As last fabrication step, the results of the single layer film fabrication are combined to obtain multilayer films containing a graded cathode and an electrolyte layer. In a first approach, a 3-layer PAD film (3.I) consisting of an NMC layer, a Composite 2 layer, and an LLZO layer was fabricated and analyzed. The resulting images including SEM and as well as a standardless EDX mapping are shown in **Figure** 4. Furthermore, the concentration curve for Ni and La throughout the three different layers is presented as net counts measured by standardless EDX.

Figure 4a illustrates the successful subsequent deposition of an NMC layer ($d \approx 8.2$ µm), a composite layer ($d \approx 15.5$ µm), and an LLZO layer ($d \approx 14.2$ µm) with PAD. Additionally, the standardless EDX analysis shows that a decreasing Ni concentration as well as an increasing La concentration toward the electrolyte layer is present within the fabricated film. The observation is supported by the BSE image in **Figure** 5b. Figure 5b reveals a homogeneous dark gray layer of NMC and a light gray layer of LLZO. In contrast, the Composite 2 displays a mixture of lighter and darker parts.

Building on these results, in a second approach, a 5-layer PAD film (3.II) including all the investigated composite materials was prepared. The results of the film analysis are shown in Figure 5. Again, the samples were analyzed by SEM (SE and BSE) and a standardless EDX mapping and a concentration profile of Ni and La in the five layers is presented.

The SEM images in Figure 5 show four different layers. The bottom layer above the substrate is the NMC layer ($d \approx 8.9$ µm), followed by the Composite 1 layer ($d \approx 14.9$ µm). As there is no clear demarcation, the third layer with a thickness of $d \approx 21.6$ µm can be assigned to the Composite 2 and 3 layers. The layer at the top can be identified as LLZO ($d \approx 12.5$ µm). This is supported by the BSE image in Figure 5b), where a homogeneous layer is observed for the first and last layers (NMC and LLZO). For the second and third layers, a mixture of two phases can be detected. Again, the darker gray within the film can be attributed to NMC and the lighter gray to LLZO. The concentration profile of Ni and La based on the EDX analysis shows an increase in La and a decrease in Ni toward the LLZO layer.

Both approaches demonstrate that a multilayer PAD film with a graded cathode layer and a covering LLZO layer can be fabricated. The thickness of the cathode layer can be adjusted to

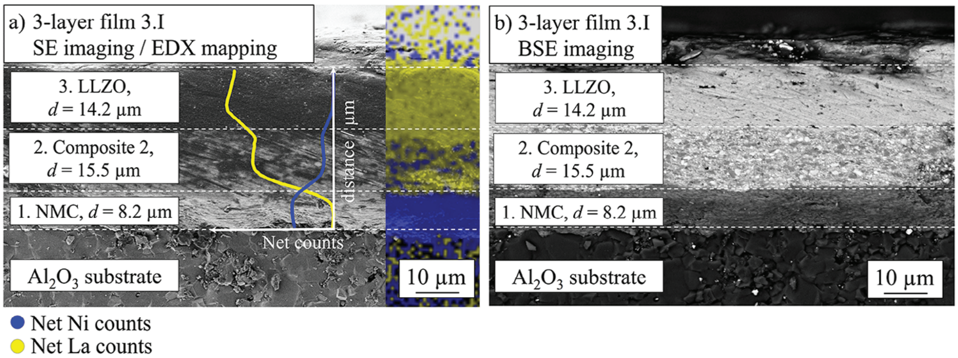

**Figure 4.** Characterization of a 3-layer PAD film (3.I) consisting of an NMC layer, a Composite 2 layer, and an LLZO layer on an $Al_2O_3$ substrate. a) SE imaging with standardless EDX mapping (Ni = blue, La = yellow) and concentration profile of Ni and La throughout the layers. b) BSE analysis.

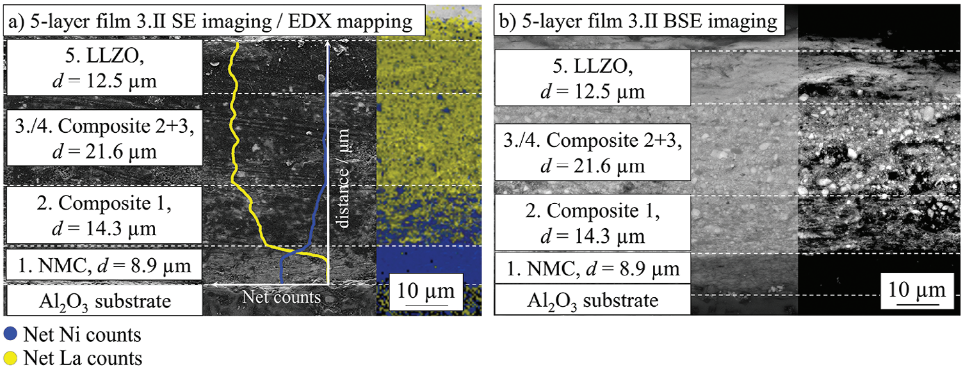

**Figure 5.** Characterization of a 5-layer PAD film (3.II) consisting of an NMC layer, a Composite 1 layer, a Composite 2 layer, a Composite 3 layer, and an LLZO layer on an $Al_2O_3$ substrate. a) SE imaging with standardless EDX mapping (Ni = blue, La = yellow) and concentration profile of Ni and La throughout the layers. b) BSE image with two different contrast levels to emphasize the different layers.

the required specification, while different film compositions in terms of NMC and LLZO concentration can be introduced as required. Furthermore, it is shown that the thickness of the raw NMC (8.2 µm vs 8.9 µm) and LLZO (14.2 µm vs 12.5 µm) layers in the two approaches is comparable, indicating good reproducibility of the deposition process.

### 3.4. Electrochemical Characterization of a PAD-ASSB (Step 4)

In **Figure 6**, the electrochemical properties of a PAD-ASSB are investigated. Therefore, a 3-layer film (cf. 3.I) consisting of a PAD-NMC ($d$ = 15 µm) and PAD-Composite 2 ($d$ = 10 µm) cathode layer, a PAD-LLZO ($d$ = 30 µm) electrolyte layer with Li metal foil as anode (cf. Figure 6a) were charged and discharged with a current of $I$ = 2 µA.

The potential curve in Figure 6b shows a change in open-circuit voltage (OCV) after each step. The impedance spectra in Figure 6c both show a slightly depressed semicircle with a marginal increase of the polarization after cycling. A quantitative investigation of the displayed spectra is conducted by the commonly used method of equivalent circuit fitting. Therefore, the model structure $R_0$–$RQ$–$W$ is assumed with an ohmic resistance ($R_0$) in series to one nonideal resistive-capacitive element ($RQ$) and a finite-space Warburg element ($W$). A detailed overview of the fitted parameters is given in Table S4 of the Supporting Information. The results reveal an increase in the resistance of the $RQ$ element by 23.5%. In comparison, the pure ohmic part of the impedance is nearly unaltered after cycling (+0.7%). The obtained phase angle of the $RQ$ element is higher than 0.96 in both spectra, denoting a highly homogeneous process with one distinct time constant, which is further supported by the distribution of relaxation times analysis (DRT) in Figure 6d, showing one dominating peak at time constants of 4.7 ms before cycling and 5.4 ms after cycling, respectively. For more details on the DRT method, the reader is referred to the literature.[55,56] The findings are contrary to what is commonly expected for battery full cells where at least two processes with diverging time constants are overlapping.[56,57]

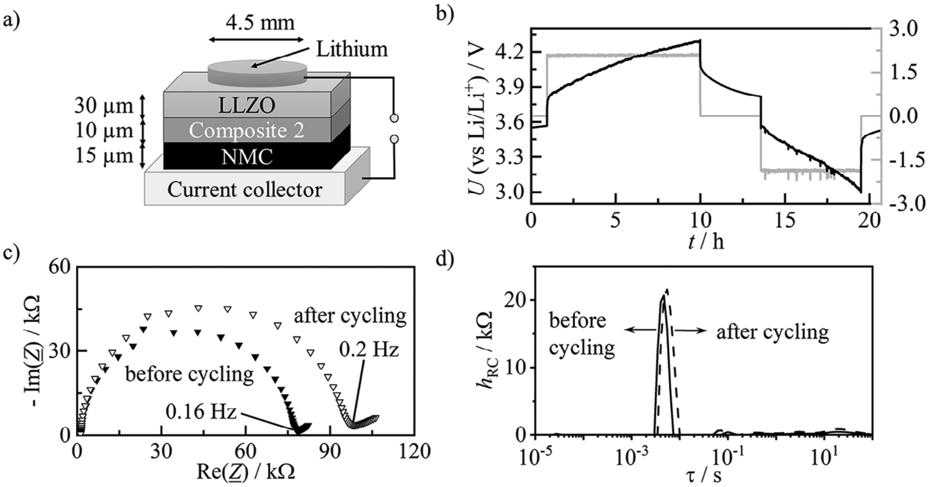

**Figure 6.** a) Schematic illustration of the electrochemically characterized PAD-ASSB cell structure. b) Potential curve (black) and applied current (gray) during cycling carried out at 70 °C. c) Impedance spectrum at 70 °C in the range of $10^4$ to $10^{-2}$ Hz before cycling (black filled triangles) and after cycling (white filled triangles). d) DRT analysis of the impedance spectra at 70 °C before cycling (straight line) and after cycling (dashed line).

The gathered data indicate that PAD-ASSBs with a PAD cathode and PAD electrolyte layer can be cycled. However, it can be assumed that in this experiment, the full potential of PAD-ASSBs cannot be utilized. The potential curve suggests a significant overpotential during charging and discharging, leading to an incomplete delithiation and lithiation of the CAM in the cathode. This is evident from the distinct decrease in voltage during relaxation. After a relaxation time of 2.5 h after charging to the cutoff voltage (4.3 V), the cell potential drops to $U_{\mathrm{ch,relax}} = 3.82$ V, although the process of relaxation is not yet complete, as implied by the slope of the voltage curve. After discharging to 3.0 V, the cell potential reaches a value of $U_{\mathrm{dch,relax}} = 3.56$ V after identical relaxation time. This indicates that the degree of lithiation of the active material is only slightly changed during cycling in this setup since the theoretical OCV window of NMC between the fully lithiated and fully delithiated state is in the range of ≈3.0–4.3 V.[58] Strong kinetic limitations in the LLZO electrolyte layer and the two cathode layers are assumed to be the reason for the insufficient utilization of active material. It might be conceivable that only the upper part of the cathode close to the electrolyte layer is engaged in the delithiation and lithiation process. Further experiments employing varying cathode layer thicknesses may provide better insight into the utilization of the CAM within the cathode layer.

The observed cell characteristics could be attributed to several intrinsic properties of PAD films in their as-deposited state. First, it is known that the RTIC mechanism, which occurs during the PAD deposition results in film stresses and high microstrain in the applied films.[8,59] It has been demonstrated on several occasions that the microstrain in PAD films has a detrimental effect on the conductivity of PAD films when compared to the properties of the corresponding bulk materials.[28,33,60,61] In addition, it should be noted that during the deposition process, the micrometer-sized particles break up into nanometer-sized fragments in the films.[8,18,59,60] The resulting nanocrystalline structure therefore provides much more grain boundaries compared to the respective bulk materials. It is known that, at least for solid electrolytes, a nanocrystalline structure with an increased amount of grain boundaries can have a negative effect on the ionic conductivity.[62,63] For CAM materials, modeling results show that although a small grain size may have a positive influence on electronic conductivity, it also impedes ion conduction.[64]

The combination of the two phenomena mentioned above seems to significantly restrict the conductive properties of the fabricated cell, resulting in high overpotential during charging/discharging and therefore limited rate capability. Based on the impedance data, it seems that only one process dominates the kinetic properties of the cell. Different studies on PAD-LLZO films demonstrate that the ionic conductivity in the as deposited state is only in the range of $10^{-8}$–$10^{-7}$ S cm$^{-1}$.[12,26,28,29] Assuming an ionic conductivity in the aforementioned range for the LLZO film within the investigated ASSB, it would be plausible that the overall impedance is dominated by the resistance of the LLZO films. However, similar studies on cathode PAD films containing NMC as CAM are currently lacking. Given the current state of the science, it is not possible to clearly identify the process and assign it to a component in the cell. Therefore, further electrochemical characterization experiments to highlight the benefits of PAD-ASSBs would not be beneficial at this stage. First, the individual components (cathode and electrolyte layer) need to be thoroughly studied to gain a deeper understanding of the impact of the characteristics of PAD-based films on the electrochemical performance. Based on these results, the film properties should then be modified toward a more suitable electrochemical performance.

## 3.5. Perspective of PAD for the Fabrication of ASSBs

### 3.5.1. Potential of PAD ASSBs

The electrochemical performance of the PAD-ASSBs examined in this study does not yet meet the requirements for commercial applications. As already mentioned earlier, only one additional study is present to date where a PAD-ASSB was fabricated and tested, showing a limited performance.[25] All in all, it is necessary to improve the overall performance of the state-of-the-art PAD-ASSBs to push the technology toward a commercial application. The beneficial properties of PAD for the fabrication of ASSBs were already described in the Introduction. Briefly summarizing these properties in terms of process control the PAD works at room temperature, no processing additives are needed and because of high film adhesion, no binder materials are necessary. In terms of cell characteristics high energy densities are possible due to high film densities and the absence of a binder material.[8,14] Adding to that, high adhesion of PAD films could be beneficial for the interfacial contact between cathode and electrolyte layer.

Based on this, the potential of PAD-ASSBs can further be highlighted with simulating possible energy densities. **Figure 7a** shows a simulation of the gravimetric ($E_{\mathrm{grav}}$, green) and volumetric ($E_{\mathrm{vol}}$, blue) energy density $E$ with respect to the cathode layer thickness. Cell characteristics considered for the simulation are listed in Table S3 of the Supporting Information. The results are compared to the energy density of a commercial LIB characterized by Günter and Wassiliadis.[65]

Figure 7a shows that $E_{\mathrm{grav}}$ of a commercial lithium-ion battery is achieved with a cathode layer thickness of 50 µm for PAD-ASSB. For $E_{\mathrm{vol}}$, this point is already reached with a cathode layer as low as 25 µm. In Figure 7b, a line profile of an NMC-PAD film is shown, where the film thickness was gradually increased. By doing so, a film thickness of ≈145 µm was obtained. In theory, PAD-ASSBs could achieve an $E_{\mathrm{grav}}$ of 417 Wh kg$^{-1}$ as well as an $E_{\mathrm{vol}}$ of 1916 Wh L$^{-1}$.

### 3.5.2. Improving the Electrochemical Performance of PAD-ASSBs

To enhance the electrochemical properties of state-of-the-art PAD-ASSBs to the energy densities mentioned above, the properties of the electrolyte layer and the cathode layer must be improved. This section discusses possible steps to improve the individual electrochemical properties of electrolyte and cathode PAD films. With respect to this study, the steps mentioned are focused on NMC as CAM and LLZO as solid electrolyte.

Starting with the solid electrolyte layer, Hanft et al. already showed that a thermal annealing of LLZO-PAD films can increase the ionic conductivity for up to 2 decades.[28] Additionally,

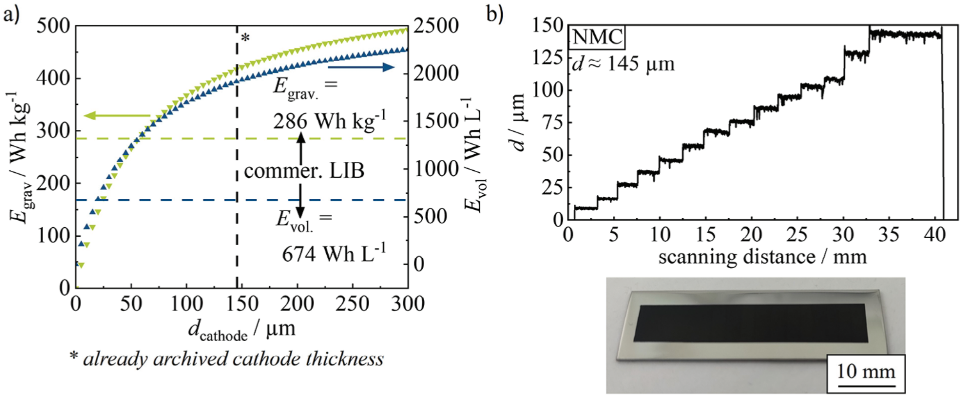

**Figure 7.** a) Simulation of the gravimetric (blue) and volumetric (green) energy density $E$ of a PAD-ASSB in respect to the cathode layer thickness. The already achieved cathode layer thickness of ≈145 µm is highlighted (black dashed line). As reference the values for $E_{grav}$ (green dashed line) and $E_{vol}$ (blue dashed line) of an commercial LIB are shown.[65] b) Line profile of an NMC-PAD film with stepwise increased film thickness up to a thickness $d \approx 145$ µm.

Nazarenus et al. showed first cycling experiments of PAD-LLZO with Li metal in a symmetrical cell setup. Yet, the cycling stability is not sufficient enough and the current densities are limited.[12] The first step should focus on decreasing interfacial resistance at the Li||LLZO interface as well as improving the cycling stability of PAD-LLZO films. To reduce the interfacial resistance, the surface of the film could be modified. Several studies have shown that the introduction of an interlayer between LLZO and Li can improve the stability of LLZO toward Li and thus decreases the interfacial resistance.[66–76] In addition, the microstructure of LLZO could be modified. As mentioned above, PAD films are nanocrystalline, resulting in an increased number of grain boundaries compared to the bulk material. Yet, it is known that Li dendrite growth preferentially takes place at the grain boundaries in LLZO films.[77–79] Therefore, it is possible that increasing the crystallite size within LLZO films could improve the cycling stability, since the amount of grain boundaries is reduced.

For the cathode layer, studies on the electrochemical performance of NMC as CAM in PAD films have shown that such films can be cycled.[15–17] However, there is a lack of research aiming for their improvement to enhance the overall electrochemical performance. A first step could be the in-depth analysis of the microstructure of a PAD cathode film. Commonly, the grain size of CAM used in cathode layers is in the µm range, while the crystallite size in PAD films does not exceed 100 nm.[80,81] It could be important to understand the impact of the increased amount of grain boundaries on the conducting performance in NMC-PAD films. As previously stated, modeling results for ion transport indicate a negative impact of small grain sizes in CAM on the conductive properties.[64] In addition to the grain size microstructure of the cathode, the microstructure of the cathode composition should be adjusted. Unlike in LIB, the electrolyte material in ASSBs cannot be introduced into the cathode layer after the fabrication of the cathode. To ensure sufficient ionic conductivity and, with that, sufficient current densities within the cathode of the ASSBs the solid electrolyte should be introduced during the cathode film fabrication.[48] Kato et al. already showed that NMC/LATP composite cathodes can be fabricated and cycled using PAD.[16] Yet, the composition still needs to be optimized with respect to overall electrochemical performance. As Clausnitzer et al. suggest that the implementation of a gradient with a decreasing amount of CAM toward the separator could be beneficial for the electrochemical properties.[48] Finally, the post-treatment of cathode PAD films with NMC as CAM must be investigated. As already described earlier, it is known that due to the deposition mechanism film stresses and high microstrain are present in the as-deposited film, which negatively influence the conducting properties.[8,28,33,59–61] Therefore, it is necessary to identify an appropriate post-treatment method to reduce the film stress and to optimize the conducting properties of cathode PAD films.

## 4. Conclusion

The identification of new processing methods for the economical fabrication of ASSBs containing ceramic materials is crucial to achieving a commercial breakthrough. In the present study, the PAD was used to demonstrate that ASSBs can be fabricated at room temperature with sufficient cell dimensions. Using NMC as CAM and LLZO as solid electrolyte, it was demonstrated that an ASSB with a graded cathode layer with increasing solid electrolyte concentration toward the electrolyte layer can be fabricated. The results were confirmed by SEM and standardless EDX analysis. In the next step, for the first time, it was demonstrated that a PAD-ASSB based on NMC as CAM can be successfully cycled using both cycling experiments and EIS. It is worth noting that, to our knowledge, there is no evidence to date that a stepped cathode has been successfully manufactured or used in a PAD-ASSB. The data obtained from the electrochemical characterization was put into perspective with the identification of the theoretical potential of PAD-ASSBs. Therefore, the possible energy densities of a PAD-ASSB were simulated and compared with the energy density of a commercial LIB. In light of these findings, the remaining challenges for PAD-ASSBs were discussed. Building on this, potential strategies to enhance the energy densities of PAD-ASSBs and bridge the gap between their practical and theoretical potential were presented.

## Supporting Information

Supporting Information is available from the Wiley Online Library or from the author.

## Acknowledgements

The authors thank the Bavarian Polymer Institute (BPI, Keylab Electron and Optical Microscopy) for providing the SEM and EDX equipment. In this regard, the authors gratefully acknowledge the contribution of M. Heider for the acquisition of the SEM images and EDX data. Support by the BayBatt Cell Technology Center is gratefully acknowledged, funded by the Deutsche Forschungsgemeinschaft (DFG, German Research Foundation) – INST 91/452-1 LAGG. The authors would like to thank the German Federal Ministry of Education and Research (BMBF) within the framework of the FestBatt2 cluster (BMBF Grant No. 03XP0441A) and the Bavarian Center for Battery Technology (BayBatt) for funding this research work.

Open access funding enabled and organized by Projekt DEAL.

## Conflict of Interest

The authors declare no conflict of interest.

## Author Contributions

L.H. performed the experiments and evaluated the results. P.W. was responsible for the film fabrication. M.L. and U.M. provided support in the evaluation of the gathered SEM and EDX data. D.P. provided detailed knowledge about PAD film characteristics. L.H. and M.S. performed the electrochemical characterization and the subsequent evaluation of the data for the battery cells. J.K., M.A.D. as well as R.M. supervised the work. L.H. and R.M. prepared the submitted the manuscript. All authors discussed the received results, have read, and agreed to the published version of the manuscript.

## Data Availability Statement

The data that support the findings of this study are available from the corresponding author upon reasonable request.

## Keywords

all-solid-state batteries, aerosol deposition method, battery fabrication, graded cathode, garnets, powder aerosol deposition method, solid electrolyte

Received: May 10, 2024
Revised: August 9, 2024
Published online: August 23, 2024

---

[1] J. Janek, W. G. Zeier, *Nat. Energy* **2023**, *8*, 230.
[2] C. Li, Z. Wang, Z. He, Y. Li, J. Mao, K. Dai, C. Yan, J. Zheng, *Sustain. Mater. Technol.* **2021**, *29*, 00297.
[3] A. Manthiram, X. Yu, S. Wang, *Nat. Rev. Mater.* **2017**, *2*, 16103.
[4] A. Varzi, R. Raccichini, S. Passerini, B. Scrosati, *J. Mater. Chem. A* **2016**, *4*, 17251.
[5] K. Kerman, A. Luntz, V. Viswanathan, Y.-M. Chiang, Z. Chen, *J. Electrochem. Soc.* **2017**, *164*, A1731.
[6] N. Boaretto, I. Garbayo, S. Valiyaveettil-SobhanRaj, A. Quintela, C. Li, M. Casas-Cabanas, F. Aguesse, *J. Power Sources* **2021**, *502*, 229919.
[7] J. Schnell, T. Günther, T. Knoche, C. Vieider, L. Köhler, A. Just, M. Keller, S. Passerini, G. Reinhart, *J. Power Sources* **2018**, *382*, 160.
[8] J. Akedo, *J. Therm. Spray Technol.* **2008**, *17*, 181.
[9] K. Žiberna, M. Šadl, A. Drnovšek, G. Dražić, H. Uršič, A. Benčan, *Crystals* **2023**, *13*, 536.
[10] J. Akedo, M. Ichiki, K. Kikuchi, R. Maeda, *Sens. Actuator A* **1998**, *69*, 106.
[11] D. Hanft, J. Exner, M. Schubert, T. Stöcker, P. Fuierer, R. Moos, *J. Ceram. Sci. Tech.* **2015**, *6*, 147.
[12] T. Nazarenus, Y. Sun, J. Exner, J. Kita, R. Moos, *Energy Technol.* **2021**, *9*, 2100211.
[13] M. Linz, J. Exner, J. Kita, F. Bühner, M. Seipenbusch, R. Moos, *Coatings* **2021**, *11*, 844.
[14] J. Akedo, *Mater. Sci. Forum* **2004**, *449–452*, 43.
[15] S. Iwasaki, T. Hamanaka, T. Yamakawa, W. C. West, K. Yamamoto, M. Motoyama, T. Hirayama, Y. Iriyama, *J. Power Sources* **2014**, *272*, 1086.
[16] T. Kato, S. Iwasaki, Y. Ishii, M. Motoyama, W. C. West, Y. Yamamoto, Y. Iriyama, *J. Power Sources* **2016**, *303*, 65.
[17] I. Kim, T.-H. Nam, K.-W. Kim, J.-H. Ahn, D.-S. Park, C. Ahn, B. S. Chun, G. Wang, H.-J. Ahn, *Nanoscale Res. Lett.* **2012**, *7*, 64.
[18] M. Linz, F. Bühner, D. Paulus, L. Hennerici, Y. Guo, V. Mereacre, U. Mansfeld, M. Seipenbusch, J. Kita, R. Moos, *Adv. Mater.* **2023**, *36*, 2308294.
[19] E. J. Cheng, Y. Kushida, T. Abe, K. Kanamura, *ACS Appl. Mater. Interfaces* **2022**, *14*, 40881.
[20] S. Muto, Y. Yamamoto, M. Sakakura, H.-K. Tian, Y. Tateyama, Y. Iriyama, *ACS Appl. Energy Mater.* **2022**, *5*, 98.
[21] T. Yamamoto, M. Motoyama, Y. Iriyama, *J. Jpn. Soc. Powder Powder Metallurgy* **2020**, *67*, 200.
[22] C.-W. Ahn, J.-J. Choi, J. Ryu, B.-D. Hahn, J.-W. Kim, W.-H. Yoon, J.-H. Choi, J.-S. Lee, D.-S. Park, *J. Power Sources* **2014**, *272*, 554.
[23] C.-W. Ahn, J.-J. Choi, J. Ryu, B.-D. Hahn, J.-W. Kim, W.-H. Yoon, J.-H. Choi, D.-S. Park, *Carbon* **2015**, *82*, 135.
[24] I. Kim, J. Park, T.-H. Nam, K.-W. Kim, J.-H. Ahn, D.-S. Park, C. Ahn, G. Wang, H.-J. Ahn, *J. Power Sources* **2013**, *244*, 646.
[25] C.-W. Ahn, J.-J. Choi, J. Ryu, B.-D. Hahn, J.-W. Kim, W.-H. Yoon, J.-H. Choi, D.-S. Park, *J. Electrochem. Soc.* **2015**, *162*, A60.
[26] T. Nazarenus, J. Schneider, L. Hennerici, R. Moos, J. Kita, *Funct. Mater. Lett.* **2023**, *16*, 2350014.
[27] R. Inada, T. Okada, A. Bando, T. Tojo, Y. Sakurai, *Prog. Nat. Sci.* **2017**, *27*, 350.
[28] D. Hanft, J. Exner, R. Moos, *J. Power Sources* **2017**, *361*, 61.
[29] M. Hahn, D. Rosenbach, A. Krimalowski, T. Nazarenus, R. Moos, M. Thelakkat, M. A. Danzer, *Electrochim. Acta* **2020**, *344*, 136060.
[30] J. Han, A. Vu, J. J. Kim, J. Gim, J. R. Croy, T. H. Lee, E. Lee, *Chem. Eng. J.* **2024**, *481*, 148645.
[31] D. Popovici, H. Nagai, S. Fujishima, J. Akedo, *J. Am. Ceram. Soc.* **2011**, *94*, 3847.
[32] R. Inada, K. Ishida, M. Tojo, T. Okada, T. Tojo, Y. Sakurai, *Ceram. Int.* **2015**, *41*, 11136.
[33] A. Khan, C.-W. Ahn, J. Ryu, W.-H. Yoon, B.-D. Hahn, J.-J. Choi, J.-W. Kim, D.-S. Park, *Met. Mater. Int.* **2014**, *20*, 399.
[34] J.-J. Choi, C.-W. Ahn, J. Ryu, B.-D. Hahn, J.-W. Kim, W.-H. Yoon, D.-S. Park, *J. Korean Phys. Soc.* **2016**, *68*, 12.
[35] T. Iida, T. Hirono, N. Shibamura, H. Sakaguchi, *Electrochemistry* **2008**, *76*, 644.
[36] H. Usui, Y. Kiri, H. Sakaguchi, *Thin Solid Films* **2012**, *520*, 7006.
[37] H. Usui, H. Nishinami, T. Iida, H. Sakaguchi, *Electrochemistry* **2010**, *78*, 329.
[38] H. Usui, K. Nouno, Y. Takemoto, K. Nakada, A. Ishii, H. Sakaguchi, *J. Power Sources* **2014**, *268*, 848.
[39] H. Usui, M. Shibata, K. Nakai, H. Sakaguchi, *J. Power Sources* **2011**, *196*, 2143.
[40] H. Usui, N. Uchida, H. Sakaguchi, *J. Power Sources* **2011**, *196*, 10244.
[41] H. Usui, N. Uchida, H. Sakaguchi, *Electrochemistry* **2012**, *80*, 737.

[42] H. Usui, K. Wasada, M. Shimizu, H. Sakaguchi, *Electrochim. Acta* **2013**, *111*, 575.
[43] D. Azuma, R. Inada, *Thin Solid Films* **2022**, *761*, 139537.
[44] T. Moritaka, Y. Yamashita, T. Tojo, R. Inada, Y. Sakurai, *Nanomaterials* **2019**, *9*, 1032.
[45] T. Esaka, H. Sakaguchi, Y. Miyashita, *Electrochemistry* **2010**, *78*, 611.
[46] H. Sakaguchi, T. Toda, Y. Nagao, T. Esaka, *Electrochem. Solid-State Lett.* **2007**, *10*, J146.
[47] J. Janek, W. G. Zeier, *Nat. Energy* **2016**, *1*, 16141.
[48] M. Clausnitzer, R. Mücke, F. Al-Jaljouli, S. Hein, M. Finsterbusch, T. Danner, D. Fattakhova-Rohlfing, O. Guillon, A. Latz, *Batter. Supercaps* **2023**, *6*, 202300167.
[49] X.-D. Zhang, F.-S. Yue, J.-Y. Liang, J.-L. Shi, H. Li, Y.-G. Guo, *Small Struct.* **2020**, *1*, 2000042.
[50] P. Minnmann, F. Strauss, A. Bielefeld, R. Ruess, P. Adelhelm, S. Burkhardt, S. L. Dreyer, E. Trevisanello, H. Ehrenberg, T. Brezesinski, F. H. Richter, J. Janek, *Adv. Energy Mater.* **2022**, *12*, 2201425.
[51] M. Clausnitzer, T. Danner, B. Prifling, M. Neumann, V. Schmidt, A. Latz, *Batter. Supercaps* **2024**, *7*, 202300522.
[52] A. Shodiev, M. Chouchane, M. Gaberscek, O. Arcelus, J. Xu, H. Oularbi, J. Yu, J. Li, M. Morcrette, A. A. Franco, *Energy Storage Mater.* **2022**, *47*, 462.
[53] Y. Qi, T. Jang, V. Ramadesigan, D. T. Schwartz, V. R. Subramanian, *J. Electrochem. Soc.* **2017**, *164*, A3196.
[54] Y. Iriyama, M. Wadaguchi, K. Yoshida, Y. Yamamoto, M. Motoyama, T. Yamamoto, *J. Power Sources* **2018**, *385*, 55.
[55] M. A. Danzer, *Batteries* **2019**, *5*, 53.
[56] C. Plank, T. Rüther, L. Jahn, M. Schamel, J. P. Schmidt, F. Ciucci, M. A. Danzer, *J. Power Sources* **2024**, *594*, 233845.
[57] C. König, A. Ramanayagam, J. Kraus, B. Roling, *Batter. Supercaps* **2024**, *7*, 202300578.
[58] D. Lu, M. S. Trimboli, G. L. Plett, *J. Electrochem. Soc.* **2022**, *169*, 07524.
[59] D. Paulus, J. Kita, R. Moos, *Ceram. Int.* **2023**, *49*, 38375.
[60] J. Exner, T. Nazarenus, D. Hanft, J. Kita, R. Moos, *Adv. Mater.* **2020**, *32*, 1908104.
[61] J. Exner, P. Fuierer, R. Moos, *Thin Solid Films* **2014**, *573*, 185.
[62] J. A. Dawson, P. Canepa, T. Famprikis, C. Masquelier, M. S. Islam, *J. Am. Chem. Soc.* **2018**, *140*, 362.
[63] S. Yu, D. J. Siegel, *Chem. Mater.* **2017**, *29*, 9639.
[64] A. Bielefeld, D. A. Weber, J. Janek, *ACS Appl. Mater. Interfaces* **2020**, *12*, 12821.
[65] F. J. Günter, N. Wassiliadis, *J. Electrochem. Soc.* **2022**, *169*, 030515.
[66] J. Dai, C. Yang, C. Wang, G. Pastel, L. Hu, *Adv. Mater.* **2018**, *30*, 1802068.
[67] H. Huo, Y. Chen, N. Zhao, X. Lin, J. Luo, X. Yang, Y. Liu, X. Guo, X. Sun, *Nano Energy* **2019**, *61*, 119.
[68] Y. Ruan, Y. Lu, X. Huang, J. Su, C. Sun, J. Jin, Z. Wen, *J. Mater. Chem. A* **2019**, *7*, 14565.
[69] X. Han, Y. Gong, K. K. Fu, X. He, G. T. Hitz, J. Dai, A. Pearse, B. Liu, H. Wang, G. Rubloff, Y. Mo, V. Thangadurai, E. D. Wachsman, L. Hu, *Nat. Mater.* **2017**, *16*, 572.
[70] K. Liu, R. Zhang, M. Wu, H. Jiang, T. Zhao, *J. Power Sources* **2019**, *433*, 226691.
[71] J. Fu, P. Yu, N. Zhang, G. Ren, S. Zheng, W. Huang, X. Long, H. Li, X. Liu, *Energy Environ. Sci.* **2019**, *12*, 1404.
[72] Y. Lu, X. Huang, Y. Ruan, Q. Wang, R. Kun, J. Yang, Z. Wen, *J. Mater. Chem. A* **2018**, *6*, 18853.
[73] A. Banerjee, X. Wang, C. Fang, E. A. Wu, Y. S. Meng, *Chem. Rev.* **2020**, *120*, 6878.
[74] H. Xu, Y. Li, A. Zhou, N. Wu, S. Xin, Z. Li, J. B. Goodenough, *Nano Lett.* **2018**, *18*, 7414.
[75] C.-L. Tsai, V. Roddatis, C. V. Chandran, Q. Ma, S. Uhlenbruck, M. Bram, P. Heitjans, O. Guillon, *ACS Appl. Mater. Interfaces* **2016**, *8*, 10617.
[76] W. Luo, Y. Gong, Y. Zhu, Y. Li, Y. Yao, Y. Zhang, K. K. Fu, G. Pastel, C.-F. Lin, Y. Mo, E. D. Wachsman, L. Hu, *Adv. Mater.* **2017**, *29*, 1606042.
[77] E. J. Cheng, A. Sharafi, J. Sakamoto, *Electrochim. Acta* **2017**, *223*, 85.
[78] Y. Ren, Y. Shen, Y. Lin, C.-W. Nan, *Electrochem. Commun.* **2015**, *57*, 27.
[79] X. Liu, R. Garcia-Mendez, A. R. Lupini, Y. Cheng, Z. D. Hood, F. Han, A. Sharafi, J. C. Idrobo, N. J. Dudney, C. Wang, C. Ma, J. Sakamoto, M. Chi, *Nat. Mater.* **2021**, *20*, 1485.
[80] P.-C. Tsai, B. Wen, M. Wolfman, M.-J. Choe, M. S. Pan, L. Su, K. Thornton, J. Cabana, Y.-M. Chiang, *Energy Environ. Sci.* **2018**, *11*, 860.
[81] J. Li, H. Li, W. Stone, R. Weber, S. Hy, J. R. Dahn, *J. Electrochem. Soc.* **2017**, *164*, A3529.